

**Supporting Information to: Hybrid Tip-Enhanced
Nanospectroscopy and Nanoimaging of Monolayer WSe₂ with
Local Strain Control**

Kyoung-Duck Park,¹ Omar Khatib,¹ Vasily Kravtsov,¹
Genevieve Clark,² Xiaodong Xu,² and Markus B. Raschke¹

*¹Department of Physics, Department of Chemistry, and JILA,
University of Colorado, Boulder, CO, 80309, USA*

*²Department of Physics, Department of Materials Science and Engineering,
University of Washington, Seattle, Washington 98195, USA*

(Dated: March 7, 2016)

POLARIZATION DEPENDENCE OF TIP PLASMON

Fig. S1a and b show experimental setup, and tip plasmon and WSe₂ PL spectra with respect to the incident polarization angle θ as defined in the inset. The incident beam is focused onto the tip apex, and the WSe₂ sample is initially located out of focus at 1 μm distance below the tip. The tip plasmon intensity is strong for P_{in} excitation ($\theta = 150^\circ$) and substantially decreased (> 10 times) for S_{in} excitation ($\theta = 60^\circ$). The far-field PL intensity of WSe₂ is not affected by the tip plasmon and the small change of intensity for the different angle results from the polarization dependent reflectivity of the beam splitter.

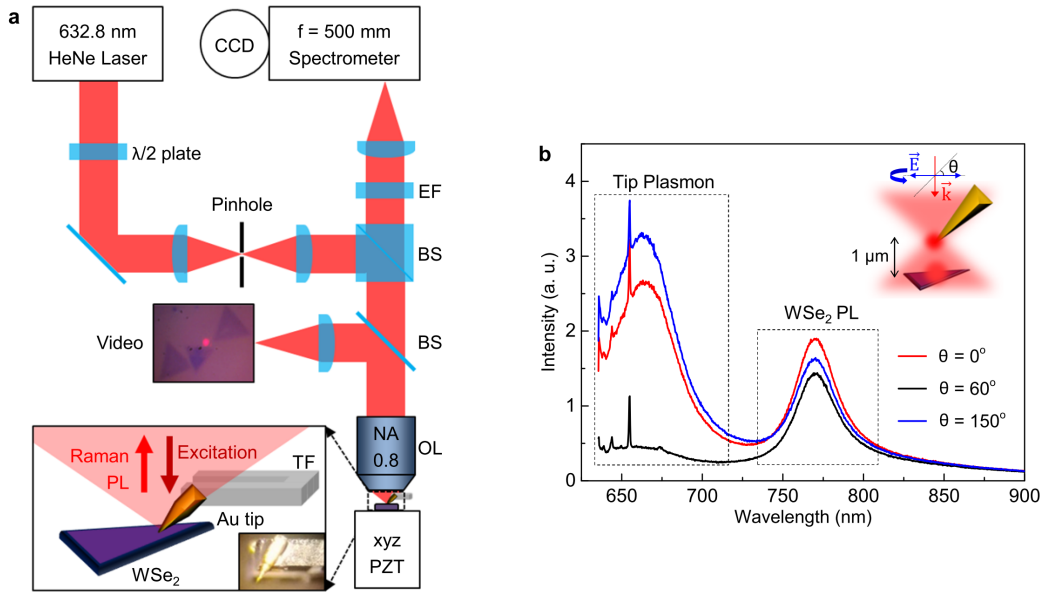


Figure S1. (a) Schematic of the multi-modal TEPL/TERS setup. EF: edge filter, BS: beam splitter, OL: objective lens. (b) Confocal far-field tip plasmon and WSe₂ PL spectra for three different polarization angles of incident laser.

DISTANCE-DEPENDENT TIP PLASMON AND PHOTOLUMINESCENCE

Fig. S2a shows tip-sample approach behavior. As the tip is closely approaching to the sample, the PL spectral intensity of WSe₂ is enhanced as shown in Fig. S2b due to near-field interaction. Notably, the tip plasmon is quenched in this regime (marked with white dashed box in Fig. S2a). This tip plasmon quenching can be possibly understood as a result of the optical excitation transfer from the tip to the WSe₂ with subsequent non-radiative decay. We find typical tip plasmon resonances in the range between 600 and 800 nm PL but not consistently for all gold tips used. However, for those tips which exhibit a tip plasmon resonance, we generally observe tip-enhanced PL of WSe₂.

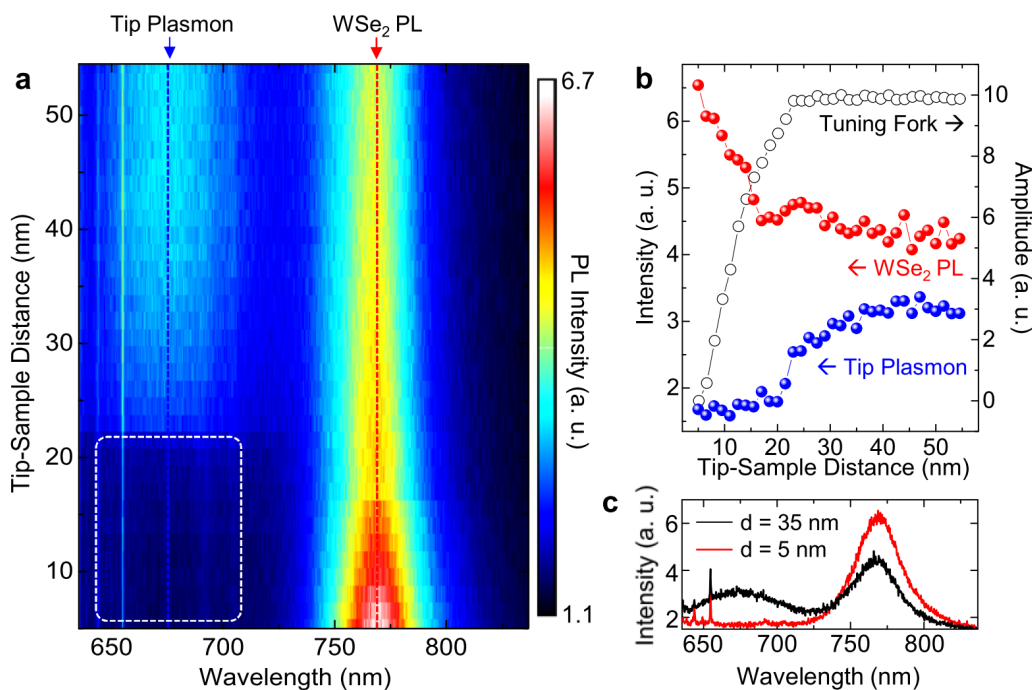


Figure S2. (a) Tip-sample distance dependence of TEPL of monolayer WSe₂. Spectra are measured in 1.5 nm increments and 0.2 s acquisition time. (b) Amplitude changes of tuning fork and the peak intensity changes of tip plasmon and WSe₂ PL (~770 nm) with respect to tip-sample distance derived from the (a). (c) Tip plasmon and WSe₂ PL spectra for the different tip-sample distances (35 nm and 5 nm).

It should be noted that biexciton peak is emerged when the tip-enhancement factor is high enough as shown in Fig. 3d. Assignment of the high energy shoulder to biexcitons is suggested based on spectral position in comparison with other studies and the emergence of

that spectral feature only when the tip-enhancement is sufficiently high, as shown in Fig. 3d, suggesting the expected super-linear excitation intensity dependence. Specifically, the ~ 50 – 60 meV separation between peaks is consistent with the energy difference between exciton and biexciton peaks as reported in the literature [1, 2]. Observation of biexcitons has been also reported in literature for CW excitation using 0.1 - 10 mW power, which translates into excitation intensities of 10^4 - 10^6 W/cm² [3, 4]. In our experiment, for the incident intensity of 10^5 W/cm², only a single exciton peak is observed in the far-field measurements (Fig. 1d). The appearance of an additional peak in the near-field, where the local excitation intensity can increase up to 10^7 W/cm² due to the local field enhancement at the tip apex on the order of 10, seems consistent with the expected super-linear dependence of biexciton emission on excitation intensity [3, 4].

RATE EQUATION MODEL FOR TEPL AND TERS

In order to describe the dependence of TEPL and TERS signals on the tip-sample distance z , we use rate equations for the excited state population of sample (P_s) and tip plasmon (P_{tip}) as described in [5]:

$$\frac{dP_s}{dt} = \Gamma_e(z) - (\Gamma_s + \Gamma_{\text{RET}}(z)) P_s + \Gamma_{\text{RET}}(z) P_{\text{tip}},$$

$$\frac{dP_{\text{tip}}}{dt} = -(\Gamma_{\text{tip}} + \Gamma_{\text{RET}}(z)) P_{\text{tip}} + \Gamma_{\text{RET}}(z) P_s.$$

Here, we take into account a spatially integrated, over the near-field probe area, distance-dependent excitation rate $\Gamma_e(z) \propto (1/(R+z))^4$, with tip apex radius R . Damping rates include radiative and non-radiative contributions $\Gamma_{s,\text{tip}} = \Gamma_{s,\text{tip}}^{\text{rad}} + \Gamma_{s,\text{tip}}^{\text{nr}}$, and the non-radiative resonance energy transfer (RET) rate $\Gamma_{\text{RET}}(z) = \Gamma_{\text{tip}}^{\text{rad}} (R_0/z)^m$, with $m = 4$ due to the reduced dimensionality and the characteristic length scale of near-field energy transfer R_0 . We solve the equations for steady state and as a function of z , and obtain the PL intensity $I_{\text{PL}}(z) \propto \eta_{\text{tip}} P_{\text{tip}} + \eta_s P_s$, where $\eta_{s,\text{tip}} = \Gamma_{s,\text{tip}}^{\text{rad}}/\Gamma_{s,\text{tip}}$ is the quantum yield of the sample and tip emission.

As shown in Fig. 1e, a good agreement between the simulation and the experimental TEPL data is found for fit parameters with tip radius $R \sim 30$ nm, damping rates and quantum yields of $1/\Gamma_s \sim 0.5$ ps, $\eta_s \sim 0.1$, $1/\Gamma_{\text{tip}} \sim 30$ fs, $\eta_{\text{tip}} \sim 0.5$, and a RET length $R_0 \sim 8$ nm. TERS intensity is simulated using the same set of parameters, but assuming very short ($1/\Gamma_s \sim 5$ fs) lifetime of the excitation, to describe the near instantaneous character of the Raman process.

MULTIMODAL IMAGING

The monolayer (ML) WSe₂ has a PL peak at ~ 772 nm (~ 1.606 eV) and the PL intensity is uniform across the crystal face region. The PL intensity is decreased in the center and edge region, and the peak position is blueshifted. To visualize the spatial heterogeneity of the PL spectrum, we plot integrated intensities for the main PL (770-805 nm) and the blueshifted PL (725-760 nm) spectrally integrated at each pixel of sample scanning as described in Fig. 2c (main text). In addition, we subtract the main PL image from the blueshifted PL image after compensating for intensity variation.

It should be noted that despite high spatial resolution TEPL images enabled by the strong localized plasmon effect (Fig. 2d-f), there is a superimposed weak homogeneous far-field background signal over micron length scale. Note also that it is difficult to obtain 15 nm resolution for large area scanning due to the different thermal expansion of tip and objective lens mounts, as well as overall drift of the scanner (~ 1 nm/min) on the time scale of such a measurement. Although reproducible 50 nm spatial resolution images were obtained in the whole crystal scanning, the presented near-field image is a composite of several $1 \mu\text{m} \times 1 \mu\text{m}$ or $2 \mu\text{m} \times 1 \mu\text{m}$ TEPL image scans to achieve the best resolution images.

Fig. S3c shows line profiles for the 770 nm PL peak and 273 cm^{-1} Raman mode (same data as Fig. 4f of main text). We estimated a spatial resolution of 15 ± 5 nm according to the general convention (distance between 5% and 95% of optical intensity at the step edge).

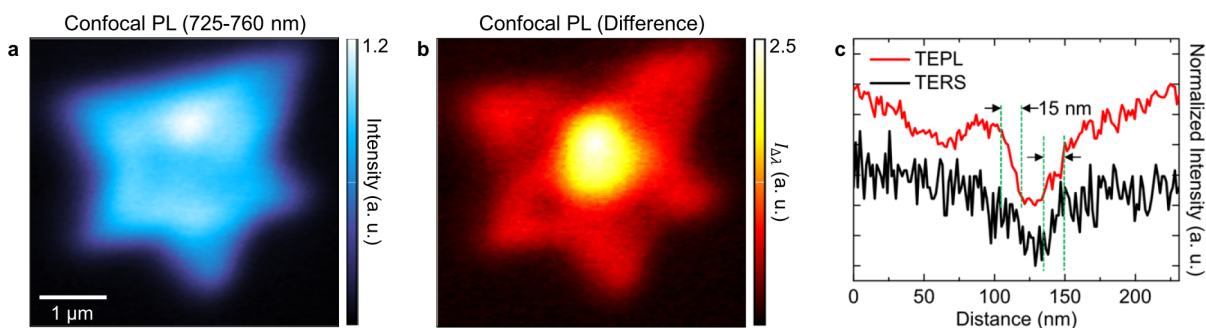


Figure S3. (a) Confocal PL image of the ML WSe₂ for the integrated intensity at 725-770 nm (blueshifted PL). Corresponding confocal PL image for the integrated intensity at 770-805 nm is shown in Fig. 2a. (b) Corresponding spectral difference confocal PL image. (c) Line profiles for the 770 nm PL peak and 273 cm^{-1} Raman mode which exhibiting 15 ± 5 nm spatial resolution.

BANDGAP ENERGY AS A FUNCTION OF STRAIN

The change of direct bandgap energy of ML WSe₂ with respect to the applied tensile strain was calculated previously using the Heyd–Scuseria–Ernzerhof (HSE) density functional theory (DFT) [6]. The bandgap energy of ML WSe₂ is found to change linearly with the tensile strain. The PL peak of the unstrained sample depends on the growth condition and substrates. Our analysis is based on the assumption of the PL peak energy of the transferred WSe₂ crystal having 0% strain. The tensile strain of as grown sample is then calculated based on the linear dependence of the PL energy with strain as shown in Fig. S4 [6].

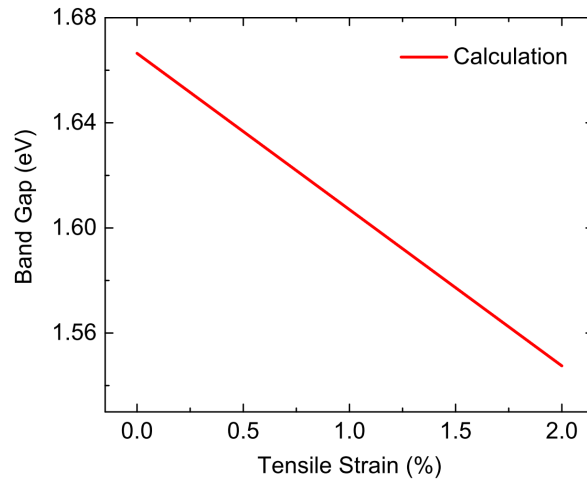


Figure S4. Calculation result for the bandgap change of ML WSe₂ with respect to the tensile strain. We assume the PL peak energy of the transferred sample has a 0% strain.

PL QUENCHING AT GRAIN BOUNDARIES

The atomic defects at the twin GBs of ML TMDs have been investigated with transmission electron microscopy (TEM) [7, 8]. These atomic defects of GBs can be further deformed or bonds broken under high strain as a result of the crystal growth procedure [7, 9]. We therefore suggest that in the previous far-field PL imaging studies, which showed clear PL decrease(increase) at the GBs of the large size TMD crystal ($> 10 \mu\text{m}$), might measure structurally deformed GBs [7, 9]. The large TMD crystals might have particularly high strain effect due to the long growth time and result in significantly large areas of PL modification at GB region. On the other hand, since the small TMD crystals have much less strain effect, PL modification is constrained to the nanoscale areas possibly dictated by exciton diffusion at the mid-gap states. In order to address this hypothesis, we perform far-field confocal PL imaging ($\sim 500 \text{ nm}$ resolution) for $\sim 10 \mu\text{m}$ size polycrystalline WSe_2 crystal, and PL quenching at GBs is clearly revealed as shown in Fig. S5a-c. It should be also noted that despite the crystal sizes are small, interflake GBs always showed distinct PL quenching due to the structural deformation as shown in Fig. S5d-f.

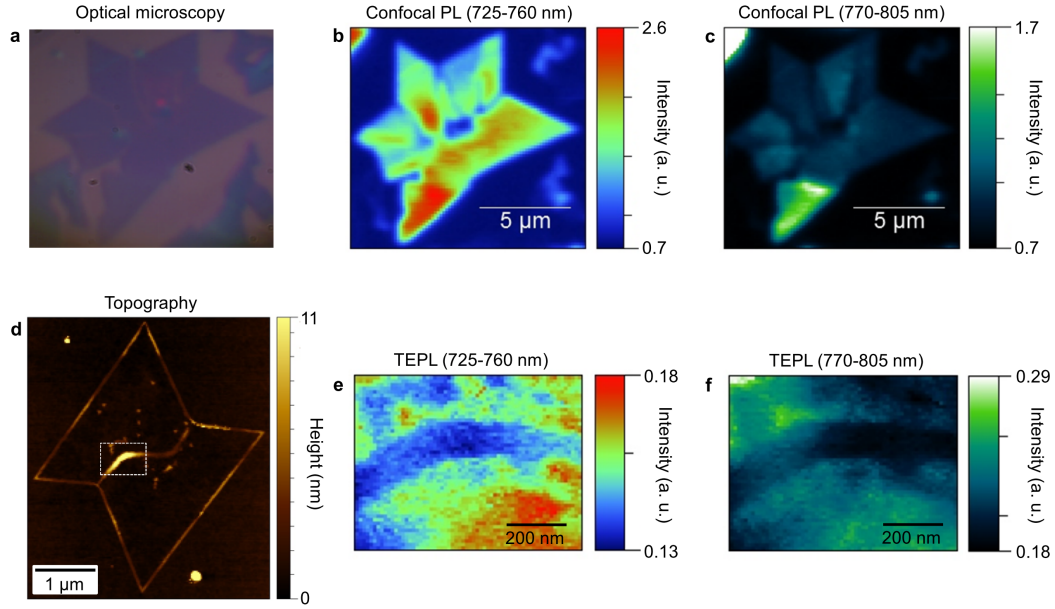


Figure S5. (a) Optical microscopy image of a polycrystalline ML WSe₂. (b) Confocal PL image for the integrated intensity at 725-760 nm spectral range. (c) Confocal PL image for the integrated intensity at 770-805 nm spectral range. (d) Topography image of the polycrystalline WSe₂ with dislocated GBs. (e) TEPL image of interflake GB region (indicated in (d) as a white dashed box) for the integrated intensity at 725-760 nm spectral range. (f) TEPL image of sample region for the integrated intensity at 770-805 nm spectral range.

-
- [1] You, Y. *et al.* Observation of biexcitons in monolayer wse2. *Nature Physics* **11**, 477–481 (2015).
 - [2] Jones, A. M. *et al.* Optical generation of excitonic valley coherence in monolayer wse2. *Nature Nanotechnology* **8**, 634–638 (2013).
 - [3] Kim, M. S. *et al.* Biexciton emission from edges and grain boundaries of triangular ws2 monolayers. *ACS Nano* **10**, 2399–2405 (2016).
 - [4] Shang, J. *et al.* Observation of excitonic fine structure in a 2d transition-metal dichalcogenide semiconductor. *ACS Nano* **9**, 647–655 (2015).
 - [5] Kravtsov, V., Berweger, S., Atkin, J. M. & Raschke, M. B. Control of plasmon emission and dynamics at the transition from classical to quantum coupling. *Nano Letters* **14**, 5270–5275 (2014).

- [6] Desai, S. B. *et al.* Strain-induced indirect to direct bandgap transition in multilayer wse₂. *Nano Letters* **14**, 4592–4597 (2014).
- [7] van der Zande, A. M. *et al.* Grains and grain boundaries in highly crystalline monolayer molybdenum disulphide. *Nature Materials* **12**, 554–561 (2013).
- [8] Najmaei, S. *et al.* Vapour phase growth and grain boundary structure of molybdenum disulphide atomic layers. *Nature Materials* **12**, 754–759 (2013).
- [9] Liu, Z. *et al.* Strain and structure heterogeneity in mos₂ atomic layers grown by chemical vapour deposition. *Nature Communications* **5**, 5246 (2014).